

Article

Low Cycle Fatigue Performance of Additively Processed and Heat-Treated Ti-6Al-7Nb Alloy for Biomedical Applications

Maxwell Hein ^{1,2,*}, David Kokalj ³ , Nelson Filipe Lopes Dias ³ , Dominic Stangier ³, Hilke Oltmanns ⁴, Sudipta Pramanik ¹, Manfred Kietzmann ⁴, Kay-Peter Hoyer ^{1,2} , Jessica Meißner ⁴ , Wolfgang Tillmann ³ and Mirko Schaper ^{1,2}

- ¹ Chair of Materials Science (LWK), Paderborn University, Warburger Str. 100, 33098 Paderborn, Germany; pramanik@lwk.upb.de (S.P.); hoyer@lwk.upb.de (K.-P.H.); schaper@lwk.upb.de (M.S.)
- ² DMRC-Direct Manufacturing Research Center, University of Paderborn, Mersinweg 3, 33100 Paderborn, Germany
- ³ Institute of Materials Engineering (LWT), TU Dortmund University, Leonhard-Euler-Str. 2, 44227 Dortmund, Germany; david.kokalj@tu-dortmund.de (D.K.); filipe.dias@tu-dortmund.de (N.F.L.D.); dominic.stangier@tu-dortmund.de (D.S.); wolfgang.tillmann@udo.edu (W.T.)
- ⁴ Department of Pharmacology, Toxicology and Pharmacy, University of Veterinary Medicine, Bünteweg 17, 30559 Hannover, Germany; hilke.oltmanns@tiho-hannover.de (H.O.); manfred.kietzmann@tiho-hannover.de (M.K.); jessica.meissner@tiho-hannover.de (J.M.)
- * Correspondence: hein@lwk.upb.de; Tel.: +49-5251-60-5447



Citation: Hein, M.; Kokalj, D.; Lopes Dias, N.F.; Stangier, D.; Oltmanns, H.; Pramanik, S.; Kietzmann, M.; Hoyer, K.-P.; Meißner, J.; Tillmann, W.; et al. Low Cycle Fatigue Performance of Additively Processed and Heat-Treated Ti-6Al-7Nb Alloy for Biomedical Applications. *Metals* **2022**, *12*, 122. <https://doi.org/10.3390/met12010122>

Academic Editors: Martin Heilmair, Martina Zimmermann and John Campbell

Received: 20 December 2021

Accepted: 7 January 2022

Published: 8 January 2022

Publisher's Note: MDPI stays neutral with regard to jurisdictional claims in published maps and institutional affiliations.



Copyright: © 2022 by the authors. Licensee MDPI, Basel, Switzerland. This article is an open access article distributed under the terms and conditions of the Creative Commons Attribution (CC BY) license (<https://creativecommons.org/licenses/by/4.0/>).

Abstract: In biomedical engineering, laser powder bed fusion is an advanced manufacturing technology, which enables, for example, the production of patient-customized implants with complex geometries. Ti-6Al-7Nb shows promising improvements, especially regarding biocompatibility, compared with other titanium alloys. The biocompatible features are investigated employing cytocompatibility and antibacterial examinations on Al₂O₃-blasted and untreated surfaces. The mechanical properties of additively manufactured Ti-6Al-7Nb are evaluated in as-built and heat-treated conditions. Recrystallization annealing (925 °C for 4 h), β annealing (1050 °C for 2 h), as well as stress relieving (600 °C for 4 h) are applied. For microstructural investigation, scanning and transmission electron microscopy are performed. The different microstructures and the mechanical properties are compared. Mechanical behavior is determined based on quasi-static tensile tests and strain-controlled low cycle fatigue tests with total strain amplitudes ϵ_A of 0.35%, 0.5%, and 0.8%. The as-built and stress-relieved conditions meet the mechanical demands for the tensile properties of the international standard ISO 5832-11. Based on the Coffin–Manson–Basquin relation, fatigue strength and ductility coefficients, as well as exponents, are determined to examine fatigue life for the different conditions. The stress-relieved condition exhibits, overall, the best properties regarding monotonic tensile and cyclic fatigue behavior.

Keywords: laser powder bed fusion; Ti-6Al-7Nb; titanium alloy; biomedical engineering; low cycle fatigue; microstructure; nanostructure

1. Introduction

Biomedical materials often are used for replacing lost or diseased biological structures [1–3]. Implants require adequate properties, including mechanical properties, such as high wear resistance, corrosion resistance, excellent biocompatibility, osseointegration, and non-cytotoxicity, to avoid revision surgeries [4].

Titanium and its alloys are generally used in biomedical applications due to their excellent biocompatibility, high corrosion resistance, and superb mechanical properties, such as low elastic modulus and high strength. Titanium alloys are the most widely used metallic materials for load-bearing biomedical applications [5–9]. Ti-6Al-7Nb is an ($\alpha + \beta$) titanium alloy with high specific strength and corrosion resistance, accompanied

by excellent biocompatibility, and is used as an orthopedic and dental alloy [10–12]. Ti-6Al-4V, which already is of high interest in the biomedical industry, is commonly used but has slight disadvantages towards Ti-6Al-7Nb, regarding corrosion resistance and biocompatibility [13]. Previous studies showed that elements such as titanium, niobium, zirconium, gold, and tin are biocompatible, whereas aluminum, vanadium, chromium, and nickel are probably hazardous elements for the human body [14,15]. Vanadium was found to be cytotoxic and there are assumptions regarding vanadium ion release in service [16,17]. Various efforts have been carried out to address the issue of cytotoxicity of the alloying elements of Ti-6Al-4V, for example, by replacing all the alloying elements, as in the alloy Ti-35Nb-7Zr-5Ta [18]. Due to the hazardous vanadium in Ti-6Al-4V, the development of Ti-6Al-7Nb, through the substitution of vanadium by niobium, offered an alternative for load-bearing implant materials [16,19,20].

Laser powder bed fusion (LPBF), also called laser beam melting, is, regarding additive manufacturing (AM) of metals, one of the most established techniques [21–23]. In LPBF processes, the fast heating rates and cooling rates, respectively, result in a characteristic microstructure and therefore characteristic mechanical properties [24–26]. Conventional fabrication methods are limited due to manufacturing constraints producing patient-specific implants. Through AM, or rather LPBF, extraordinary biomedical implant topologies, such as porous and foam structures, are feasible [27–29].

Many available research results focus on the mechanical properties of different additively manufactured alloys, such as 316L, 17-4 PH, or Ti-6Al-4V [30,31]. However, there remains a significant gap in terms of fatigue properties analysis, since most available research on dynamic behavior is related to high cycle fatigue (HCF) testing and the crack growth analysis of additively manufactured parts of steel alloys [32–36] and titanium alloys [37–42]. Only few studies deal with the low cycle fatigue (LCF) properties of additively manufactured alloys in general [43–47]. Even fewer studies were performed with a focus on post-treatments for titanium alloys. Previous studies addressed the fatigue behavior of additively processed Ti-6Al-4V for different conditions and loading situations [38,42,48,49]. Examinations of the quasi-static behavior of Ti-6Al-7Nb are at hand but none of them include LCF behavior [17,50–53]. In previous studies, extremely high loads were reported during stumbling. Such load peaks during uncontrolled movements are difficult to investigate systematically. Implants are usually examined for high cycle fatigue, although the rare extreme loads could endanger the implant. Therefore, in addition to monotonic material characterization and high cycle fatigue tests, implants should also be investigated at low cycles with higher load levels [54,55]. Given that the physiological—sometimes extreme—loading during service life as an implant is cyclic, the fatigue performance of laser beam-melted Ti-6Al-7Nb requires attention. To combine LPBF with the promising quasi-static properties of Ti-6Al-7Nb, the microstructural and mechanical properties of additively manufactured Ti-6Al-7Nb in different conditions are investigated in this work. Heat treatments are an additional part of this examination, to initiate microstructural changes for the relaxation of the tensed crystal lattice and the beneficial crack growth behavior, as well as to achieve a homogenous, decreased residual stress state [56–58]. Generally, titanium alloys are heat-treated due to high residual stresses as well as due to the brittle α' -phase, occurring after LPBF. Moreover, thermal post-treatments induce an improvement of the quasi-static mechanical properties of different titanium alloys [52,59]. To sum up, since there is a lack of studies addressing fatigue behavior, it is necessary to focus on an investigation of the microstructure under different conditions, as-built and heat-treated, and their effect on quasi-static and LCF behaviors.

2. Materials and Methods

2.1. Manufacturing Procedure, Materials, and Mechanical Characterization

The specimens were fabricated using an LT12 SLM machine (DMG MORI AG, Bielefeld, Germany) with a beam spot size of 35 μm . For data preparation, the software Materialise Magics (Version 21.1, Materialise GmbH, Munich, Germany) was applied. To

obtain dense material with LPBF (relative density $\varphi > 99.9\%$), the following parameters were used: laser power $P = 227$ W, laser scanning speed $v = 1.675$ mm s⁻¹, hatch distance $h = 0.077$ mm. A constant scanning strategy of 5 mm stripes by layer-wise rotation of the scanning vectors of 67° alongside a defined layer thickness of 50 μm was applied. As contour parameters, a laser power $P_c = 123$ W and a scanning speed $v_c = 0.512$ mm s⁻¹ were applied. The Ti-6Al-7Nb powder is supplied by ECKART TLS GmbH (Bitterfeld, Germany). The Ti-6Al-7Nb powder particles were examined concerning particle size distribution (PSD) with a Mastersizer 2000 (Malvern Panalytical GmbH, Kassel, Germany) using laser diffraction. The powder batch had a nominal PSD comprising 26.9 μm (D_{10}) and 52.1 μm (D_{90}) with a log-transformed normal distribution centered at 37.6 μm (D_{50}), see Figure 1a. Different heat treatments were performed under a vacuum atmosphere. Recrystallization annealing (HT1 = 925 °C for 4 h) was conducted to obtain equiaxed α with β at grain boundary triple points, β annealing (HT2 = 1050 °C for 2 h) to receive Widmanstätten $\alpha + \beta$ colony structures, and stress relieving (HT3 = 600 °C for 4 h) to decrease the undesirable residual stresses due to the LPBF process, as well as a decomposition of the martensitic α' to α -phase [59,60]. The heat treatment process routes are presented in Figure 1c. The powder morphology was investigated employing the scanning electron microscope (SEM) Zeiss Ultra Plus (Carl Zeiss AG, Oberkochen, Germany). The powder consists of mainly spherical particles with a few agglomerations on bigger particles, see Figure 1b. Microstructural investigations were accomplished with the SEM equipped with an electron backscatter diffraction (EBSD) unit to detect phases and corresponding grain orientations. EBSD data was post-processed using the MATLAB-based (Version R2019a 9.6, The MathWorks, Inc., Natick, MA, USA) toolbox MTEX (Version 5.6.0) [61]. MTEX is a free available toolbox for analyzing and modelling crystallographic textures. Microscopic observations and classification of the fractured surfaces for quasi-static and fatigue tests were also carried out using SEM. Microstructural study of samples on nanoscale was undertaken by transmission electron microscopy (TEM). For TEM, thin-slice samples (≈ 400 μm) were cut by Struers Sectom-5 (Struers GmbH, Willich, Germany) and further polished to a thickness of ≈ 100 μm. At last, 3 mm diameter circular disc samples were punched from the thin samples. Twin jet electropolishing of the thin foils was performed with the Struers Tenupol-5 (Struers GmbH, Willich, Germany) using an electrolyte containing perchloric acid (60 mL), butanol (340 mL), and methanol (600 mL). Electropolishing was executed at a voltage of 21 V, a current of 35 mA, and a temperature of -22 °C. TEM investigations were executed using a cold field emission gun equipped with JEOL JEM-ARM 200F (JOEL Ltd., Tokyo, Japan). TEM, high-resolution TEM (HRTEM), and high-angle annular dark-field scanning transmission electron microscopy (HAADF-STEM) images were taken. Energy dispersive spectroscopy (EDS) was performed during HAADF-STEM imaging. EDS maps were collected with a 30 nm step size with 10 s dwell time per step. The crystalline phase composition of Ti-6Al-7Nb was characterized through X-ray diffraction (XRD; D8 Advance, Bruker, Madison, WI, USA) using a Cu-K α radiation source ($\lambda = 0.154187$ nm) operating at a current of 40 mA and a voltage of 35 kV. The as-built and heat-treated Ti-6Al-7Nb parts were measured in θ - θ geometry within a scanning range from $2\theta = 30^\circ$ to $2\theta = 90^\circ$ applying a step width of 0.035° and an exposure time of 1.5 s per step. All tests for mechanical characterization were performed at an ambient temperature. Tensile specimens were built according to Figure 1d. The loading direction was parallel to the building direction (BD) of the samples.

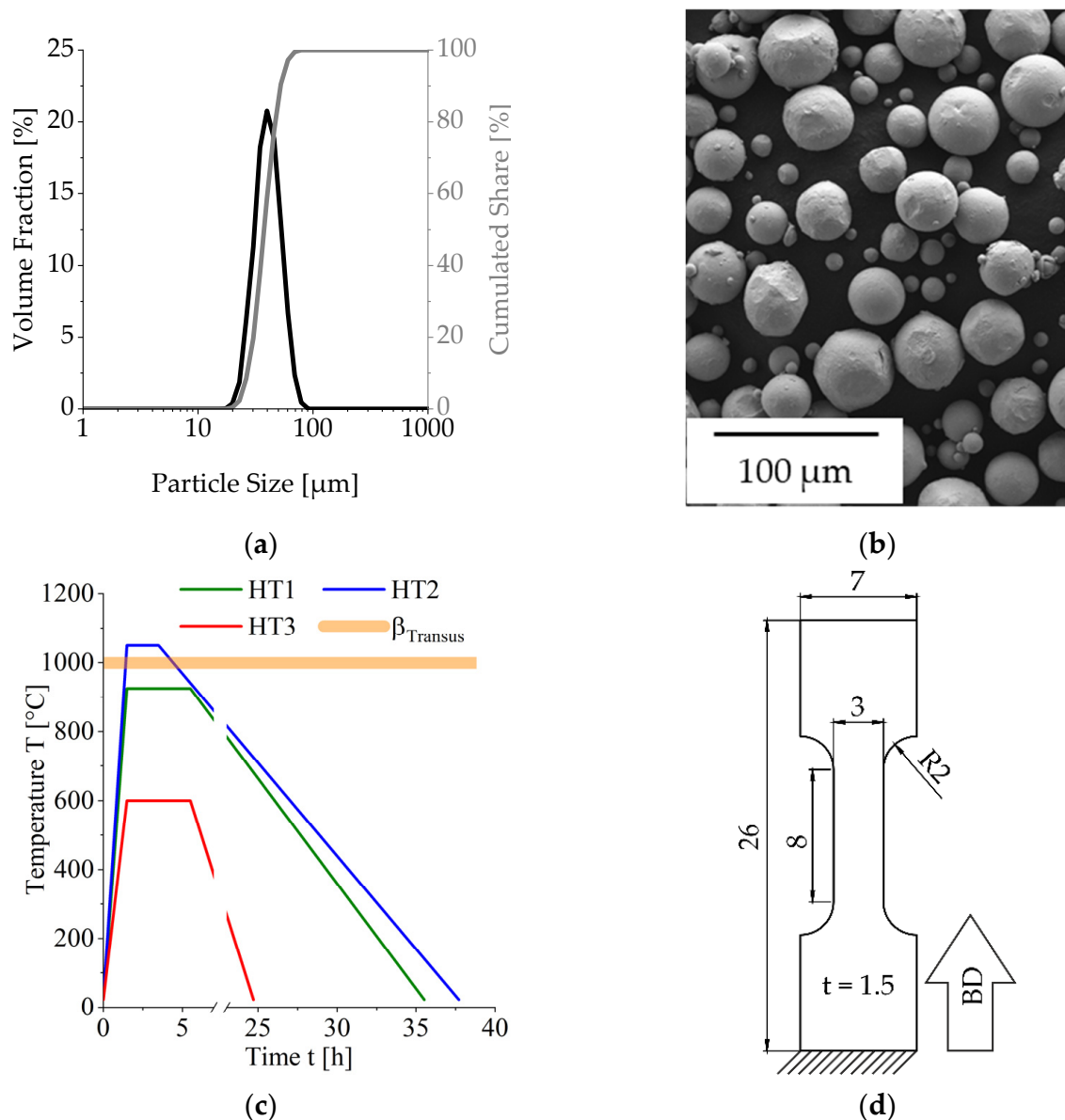


Figure 1. (a) Particle size distribution of Ti-6Al-7Nb; (b) powder morphology (SEM image); (c) schematic overview of the different heat treatments conducted—recrystallization annealing (HT1), β annealing (HT2), and stress relieving (HT3), as well as the β_{transus} temperature for the alloy; (d) geometry and building direction (BD) of tensile and fatigue specimens.

All tensile specimens were blasted with high-grade Al_2O_3 . The blasting material corresponded to a particle size of $70\ \mu\text{m}$ – $250\ \mu\text{m}$, used at 4 bar air pressure with a SMG 25 DUO (MHG Strahlanlagen GmbH, Düsseldorf, Germany). The tensile and LCF tests were performed utilizing a servo-hydraulic test-rig MTS 858 table-top system (MTS Systems Corporation, Eden Prairie, MN, USA) equipped with a 20 kN load cell and an extensometer 632.29F-30 (MTS Systems Corporation, Eden Prairie, MN, USA). The tensile test procedure corresponded to a displacement-controlled execution with a crosshead speed of $1.5\ \text{mm}\ \text{min}^{-1}$, according to DIN EN ISO 6892-1. The LCF tests were strain-controlled, at total strain amplitudes ϵ_A of 0.35%, 0.5%, and 0.8%, with a R-ratio of -1 (compression–tensile fatigue), and a strain rate of $6 \times 10^{-3}\ \text{s}^{-1}$. At least three specimens per condition were tested with both monotonic and cyclic tests for each strain amplitude. The monotonic material properties, such as Young’s moduli E , tensile yield strengths $R_{p0.2}$, ultimate tensile strengths R_m , and plastic elongations A , were obtained from the static tensile test. The determination

of the fatigue material constants requires the performance of several fatigue tests under cyclic loading and a R-ratio of -1 . Cyclically loaded materials often have unstable and changing stress amplitude during the test, due to cyclic hardening or softening. Therefore, the stress amplitude for the stabilized state must be used, which occurs at the half number of cycles to fracture. The plastic strain amplitude can either be calculated with the stress amplitude, the Young's modulus and the total strain amplitude (see Equation (4)), or by measuring the thickness of the recorded stable hysteresis loop recorded during the fatigue tests [62–65]. For evaluation of the total stress amplitude, σ_a , from the S–N curves, the Basquin relation is suitable, as follows:

$$\frac{\Delta\sigma}{2} = \sigma_a = \sigma'_f \cdot (2N_f)^b. \quad (1)$$

In Equation (1), σ'_f delineates the fatigue strength coefficient and b is the fatigue strength exponent. This equation fits the high-stress and low-stress fatigues [66]. For a better description of the high-stress fatigue region, the dependence between the number of reversals to failure $2N_f$ and the plastic strain amplitude $\Delta\varepsilon_p/2$, also called the Coffin–Manson relation, is used to describe the total fatigue life, as follows:

$$\frac{\Delta\varepsilon_p}{2} = \varepsilon'_f \cdot (2N_f)^c, \quad (2)$$

with the fatigue ductility coefficient, ε'_f , and the fatigue ductility exponent, c [66–68]. The total strain amplitude, $\Delta\varepsilon_A/2$, can be divided into two components, the plastic strain amplitude, $\Delta\varepsilon_p/2$, and the elastic strain amplitude, $\Delta\varepsilon_e/2$. The total strain amplitude, $\Delta\varepsilon/2$, of fatigue life curves is described as the sum of elastic and plastic strain amplitude, as follows, by Suresh [69]:

$$\frac{\Delta\varepsilon_A}{2} = \frac{\Delta\varepsilon_e}{2} + \frac{\Delta\varepsilon_p}{2}. \quad (3)$$

$\Delta\varepsilon_e/2$ is described by Hooke's law as the quotient of σ_a to the Young's modulus E as follows:

$$\frac{\Delta\varepsilon_e}{2} = \frac{\Delta\sigma}{2E} = \frac{\sigma_a}{E}. \quad (4)$$

Together with the modified Basquin equation and the Coffin–Manson relation, combining Equations (1)–(4), one obtains the following:

$$\varepsilon_A = \frac{\sigma'_f}{E} \cdot (2N_f)^b + \varepsilon'_f \cdot (2N_f)^c. \quad (5)$$

The first and second terms on the right-hand side of Equation (5) are the elastic ε_e and plastic ε_p components, respectively, of the total strain amplitude ε_A . Equation (5) can be used as the basis for the strain life approach to fatigue design. For determination of the fatigue life, a schematic illustration of the as-built condition is presented in Figure 2. The intersection of the curves for ε_e and ε_p describes the transition point, where the plastic and elastic strains are identical. From this point, the LCF life is governed more by elastic than plastic strain. For the as-built condition this point is around 110 cycles, see Figure 2. According to the Coffin–Manson–Basquin approximation, one is able to predict the fatigue life depending on the applied strain amplitude for the different conditions [66–68,70].

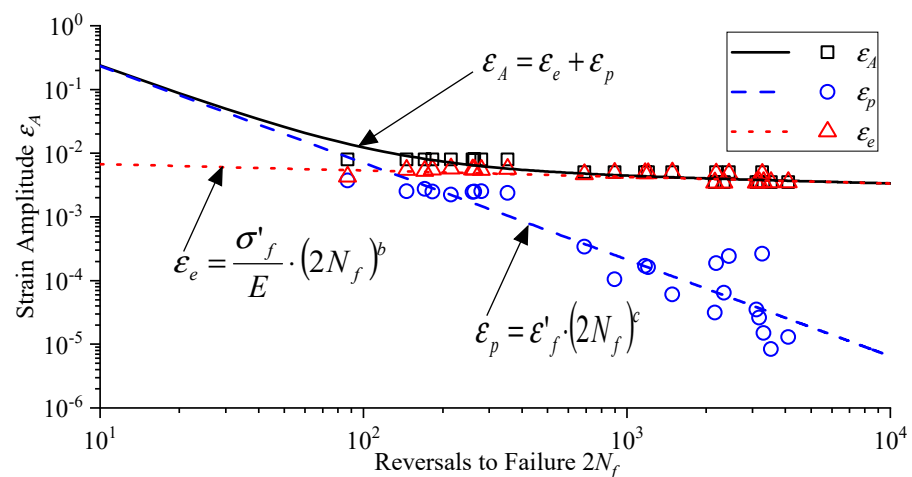


Figure 2. Example of the Coffin–Manson–Basquin curve according to Equation (5) for the as-built condition.

2.2. Biocompatibility Investigations

Two different surface conditions were analyzed to determine the optimum surface roughness for biocompatibility. On the one hand, the as-received surface was investigated without any post-treatment (NT). On the other hand, the surface was post-treated utilizing blasting with high-grade Al_2O_3 (ab). Blasting lead to rougher surfaces and to an increased surface area, resulting in faster osseointegration and higher survival rates for moderately rough implant surfaces: this was demonstrated by clinical studies [71–75]. The surface roughness was measured with an optical 3D macroscope VR-3100 (KEYENCE GmbH, Neu-Isenburg, Germany). The arithmetical mean roughness, R_a , and average roughness, R_z , were determined on the surfaces of the untreated and blasted specimens. A total of 5 specimens per condition were measured with 5 line measurements (length ≈ 6.8 mm) per side.

2.2.1. Cytocompatibility Testing

Biocompatibility studies were performed with different cell types. Therefore, murine fibroblasts (L-929; CLS Cell Lines Service, Eppelheim, Germany), human osteosarcoma cells (HOS 87070202; European Collection of Authenticated Cell Cultures, Merck, Germany), and human umbilical vein endothelial cells (HUVEC; Promocell, Heidelberg, Germany) were used. L-929 cells were grown and passaged in RPMI-1640 medium (Biochrom GmbH, Berlin, Germany), while HOS cells were grown and passaged in Eagle's MEM (EMEM)/Hanks' (Carl Roth GmbH + Co. KG, Karlsruhe, Germany). Both media were supplemented with fetal calf serum (FCS) superior (10%, Biochrom GmbH, Berlin, Germany) and penicillin/streptomycin (1%, Biochrom GmbH, Berlin, Germany). The EMEM/Hanks' medium was also supplemented with non-essential amino acids (1%, Biochrom GmbH, Berlin, Germany) and L-glutamine (2 mmol, Biochrom GmbH, Berlin, Germany). HUVEC cells were grown and passaged in an endothelial cell grown medium kit (Promocell, Heidelberg, Germany) and were supplemented with penicillin/streptomycin (1%). All cell lines were grown and passaged in cell culture flasks or multi-well plates (Greiner Bio-One, Frickenhausen, Germany). For passaging, a trypsin (0.05%)/ethylene-diamine-tetraacetic (0.02%) acid solution (Biochrom GmbH, Berlin, Germany) was used. The cells were plated with a density of 50,000 cells per well in 24-well culture plates. After hot air sterilization of the test samples, the cells were seeded on the top of the samples ($\approx 5 \times 5 \text{ mm}^2$), which were embedded in agarose (2%, Agarose NEEO, Carl Roth GmbH + Co. KG, Karlsruhe, Germany) in respective culture mediums. After 72 h incubation (in a humidified atmosphere at 37°C and 5% CO_2), cell proliferation was determined. Therefore, a crystal violet staining (CV) assay was performed [76]. After 72 h, the cells were fixed with glutaraldehyde (2%, Sigma-Aldrich, Merck KGaA, Darmstadt, Germany) in phosphate-buffered saline (PBS)

for 20 min. Subsequently, the supernatant was removed, and the cells were stained with CV (0.1%, Carl Roth GmbH + Co. KG, Karlsruhe, Germany) in deionized water. After 30 min, the pigment was removed, and the samples were removed from the agarose. After washing with deionized water, the test samples were air-dried. For 1 h, Triton X-100 (2%, Sigma-Aldrich, Merck KGaA, Darmstadt, Germany) in deionized water was added, so that CV was dissolved from the cells. Finally, the supernatant was transferred in a 96-well microtiter plate and the absorbance was determined at 570 nm using a 96-well microplate reader (MRX microplate reader, Dynatech Laboratories, Denkendorf, Germany). The experiments were carried out six times. Furthermore, the supernatant of L-929 and HOS was analyzed of the cytokine Il-6 expression (R&D Systems DuoSet, R&D Systems Inc., Minneapolis, MN, USA).

2.2.2. Antibacterial Examinations

To analyze the bacterial behavior on test samples, two different samples were used—*Escherichia coli* (ATCC 25922) and *Staphylococcus aureus* (ATCC 25923). The bacteria were cultivated on Columbia agar plates with sheep blood (7%, Fisher Scientific GmbH, Schwerte, Germany) for 24 h. The test samples were also embedded in agarose (2%, Agarose LM, Gerbu Biotechnik GmbH, Gailberg, Germany). Bacteria (10^{-6} CFU ml⁻¹) were seeded on the test samples. After 48 h of incubation at 37 °C, cell proliferation was analyzed, similarly to the cell proliferation, with a CV assay. The experiment was performed in four biological replicates.

3. Results and Discussion

3.1. Microstructure and Nanostructure of as-Built and Heat-Treated Ti-6Al-7Nb

The microstructure of ($\alpha + \beta$) titanium strongly depends on the cooling rates and the quenching parameters, from the β -phase field at higher temperatures and the following heat treatment, respectively [77,78]. Figure 3 shows EBSD maps of the Ti-6Al-7Nb alloy after additive manufacturing and subsequent heat treatments. The EBSD map of the additively processed Ti-6Al-7Nb shows a very fine, acicular microstructure, see Figure 3a,c. The fine-lamellar α' grain structures are strongly oriented inside the prior β grains. The size of these fine needles decreased with an increased cooling rate during solidification [37,79,80]. Figure 3b shows the reconstructed parent β grains using MTEX software. During solidification, the bcc β -phase preferentially grows in the $\langle 100 \rangle$ direction; therefore, the elongated, columnar primary β grains evolve parallel to the BD [81–83]. The resulting anisotropy and primary β grains affect the mechanical properties of the specimens [84]. Due to the fast cooling and passing the β_{Transus} temperature, these β grains transform to α' -phase, according to the Burgers relation, in 12 possible transformation variants [81,85–87]. Due to the high cooling rate, the probability of α' formation is very high [37,88,89]. The rapid cooling leads to a martensitic transformation and a limitation of diffusional transformation [90]. Figure 3c shows the cross-section perpendicular to the BD. Areas with similar crystallographic orientations are observable inside the grain boundaries of the probable parent β grains. Figure 3d demonstrates the microstructure for post-treatment HT1. An unexpected, coarse lamella-like microstructures evolved instead of equiaxed grains [60]. The microstructure is dependent on the initial microstructure and dislocations before the heat treatment. HT2 results in a coarse microstructure and huge grains due to temperatures above β_{Transus} and grain growth. The grain orientation seems random, see Figure 3e. Figure 3f exhibits the microstructure after stress relief treatment (HT3). Only minor changes in the microstructure occurred compared with the as-built condition. Areas with similar grain orientation are present and the prior β grain boundaries are noticeable. The detected phase distribution of α , α' , and β titanium, respectively, is summarized in Table 1.

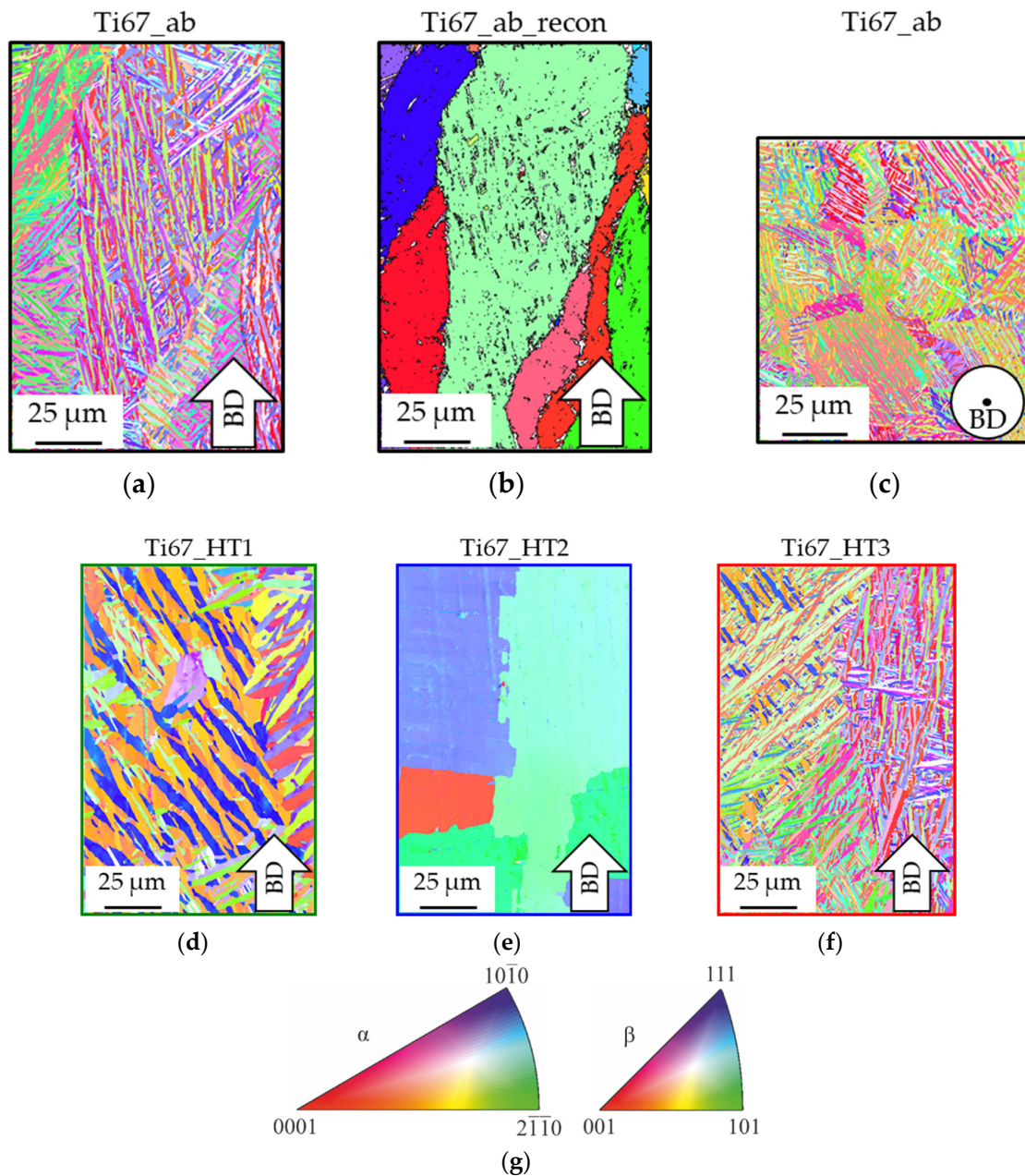


Figure 3. (a) Inverse pole figure (IPF) of as-built Ti-6Al-7Nb; (b) β parent grain reconstruction of (a); IPF of as-built (top view) (c); HT1 (d); HT2 (e); and HT3 (f) Ti-6Al-7Nb; and (g) color legend for inverse pole figure.

Figure 4 summarizes the TEM images, the HRTEM images, and the fast Fourier transformation (FFT) pattern of the as-built sample. The α' martensite laths are visible in Figure 4a. The width of the lath (dark contrast in Figure 4a) is 280 nm. Figure 4b is the FFT pattern from the white circular area in Figure 4a. Figure 4c is the FFT pattern from the yellow circular area in Figure 4b. The diffraction pattern confirms the hexagonal crystal structure of α' martensite in both laths. In addition, an HRTEM image of the interface between two laths (black square region in Figure 4a) is presented in Figure 4d. The red line highlights the interface between the two α' martensite laths. Figure 4e is the magnified HRTEM image of the black square region in Figure 4d. The $(0\bar{1}1)$ plane of one lath intersects the $(\bar{1}010)$ plane of another lath at 45° . Furthermore, Figure 4f shows the HAADF-STEM image and Figure 4g the EDS maps of the as-built sample. Here, laths of

α' martensite are apparent. The EDS maps of the black square region in Figure 4g show that no segregation of alloying elements is observable, and the titanium, aluminum, and niobium distribution is homogenous in the laths.

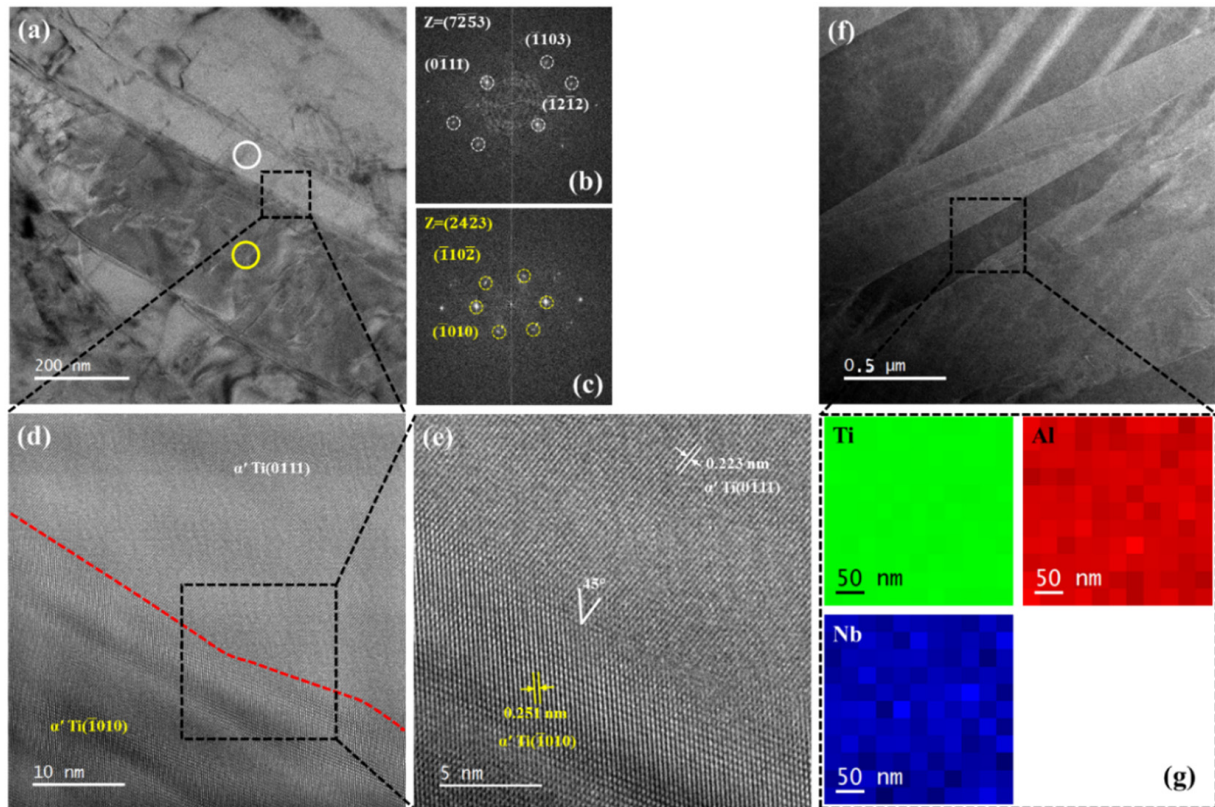


Figure 4. (a) TEM image of the as-built sample; (b,c) FFT pattern taken from the white and yellow circular areas in (a); (d) HRTEM image of the black square region in (a), the red line shows the boundary between two α' -martensite laths; (e) HRTEM image of the black square region in (d); (f) HAADF-STEM image of the as-built sample; (g) EDS maps of the black square region in (f).

Figure 5 shows the TEM images, HRTEM images, and diffraction pattern of the HT3 sample. The α laths are apparent in Figure 5a. In Figure 5a, some α laths are relatively coarse (≈ 170 nm). However, the α laths are relatively fine (≈ 40 nm). In this context, Figure 5b shows an HRTEM image taken from the region within the black square in Figure 5a. The lattice plane of two α laths is identified as $(\bar{1}010)$. The red lines point out the boundary between two α laths. For a deeper insight, Figure 5d is the magnified view of the black square region in Figure 5b. The interplanar spacing of the $(\bar{1}010)$ planes are measured as ≈ 0.252 nm. However, the two $(\bar{1}010)$ planes are misoriented by 18° . The diffraction pattern in Figure 5c confirms the zone axis to be $(\bar{1}2\bar{1}1)$. Again, the diffraction pattern shows the $(\bar{1}010)$ planes to be misoriented by 18° . Figure 5e shows the HAADF-STEM image and EDS maps of the stress relief treated sample, where α laths are visible. Finally, Figure 5f is the EDS maps of a triple junction between three α laths from the black square region in Figure 5e. An enrichment of niobium and a depletion of aluminum is observed at the triple junction. The α lath boundary regions are enriched in niobium and depleted in aluminum. This leads to the white contrast in the HAADF-STEM image in Figure 5e.

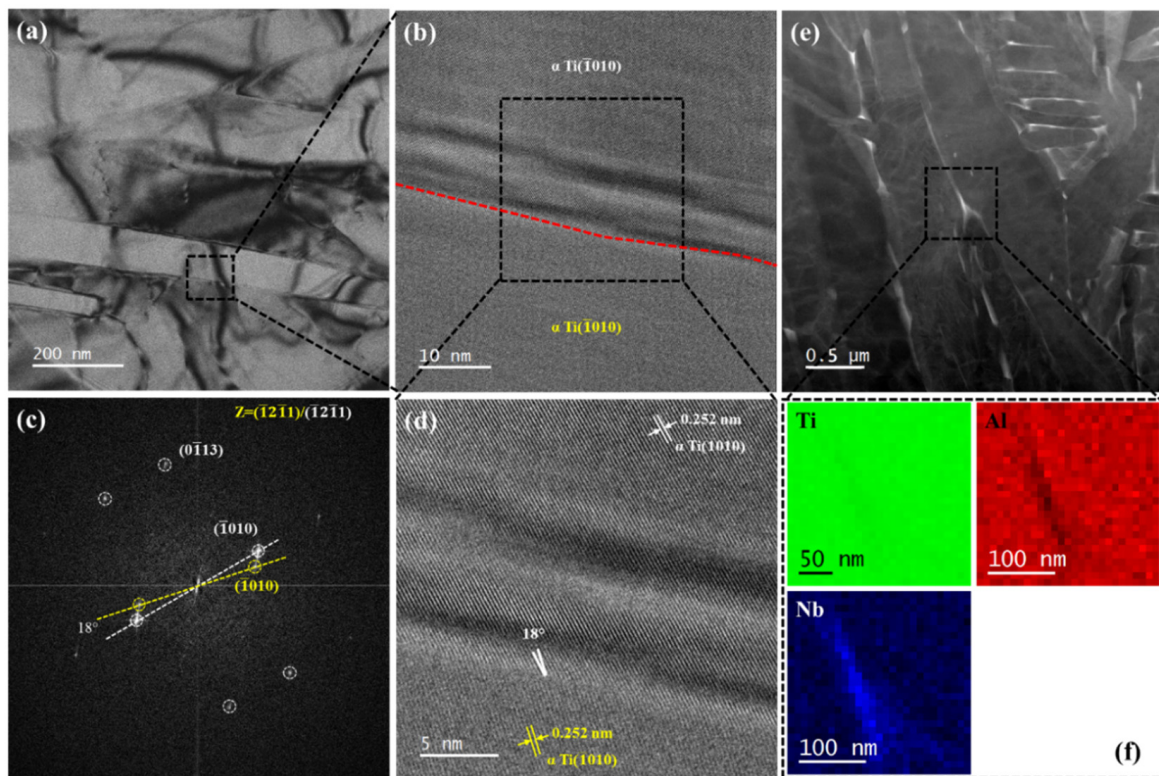


Figure 5. (a) TEM image of the HT3 sample; (b) HRTEM image from the black square area in (a), the red line indicates the boundary between two α -laths; (c) FFT pattern from the black square area in (b); (d) HRTEM image from the black square in (b); (e) HAADF-STEM image of the HT3 sample; (f) EDS maps of black square region in (e).

Figure 6 shows XRD patterns for the as-built and heat-treated Ti-6Al-7Nb samples. The XRD pattern of the sample in the as-built condition is characteristic for the hexagonal close-packed (hcp) α' / α structure of titanium alloys. Due to the hexagonal structure of both the α' and α phases with similar lattice parameters, a separation or distinction between both phases based on XRD is not possible [59]. Since additively manufactured alloys are characterized by high local cooling rates, the α' martensitic phase is assumed as dominating component, based on the findings of Xu et al. [52]. Stress relief heat treatment at 600 °C does not lead to any significant microstructural changes in the sample HT3, since the $\alpha' \rightarrow \alpha + \beta$ transformation is known to start at higher temperatures (≈ 760 °C) [59]. As shown for sample HT1, recrystallization annealing at 925 °C leads to the formation of the bcc β -structure of Ti and probably to a decomposition of α' to α . HT2 treatment was carried out above the β_{Transus} temperature and did result in decomposition of the as-fabricated α' / α -phase [59]. Therefore, the β -phase is formed in the HT2 treated specimens. This is in good agreement with reported transformations and temperatures between 735 °C and 1050 °C for the $\alpha \rightarrow \beta$ reaction [59]. Post-treatment HT1 and HT2 lead to a decrease in the α' / α -Ti peak width, indicating grain growth. For the samples HT1 and HT2 additional peaks were observed between $2\theta = 42\text{--}45^\circ$. Due to the large width of the peaks, several similar phases with small differences in stoichiometry are most likely. As reported by Bolzoni et al., titanium and aluminum can form binary phases, e.g., titanium aluminates, above 660 °C due to diffusion processes [91]. Therefore, the formation of small fractions of Ti_3Al , TiAl , and/or TiAl_3 is concluded for the heat treatments HT1 and HT2.

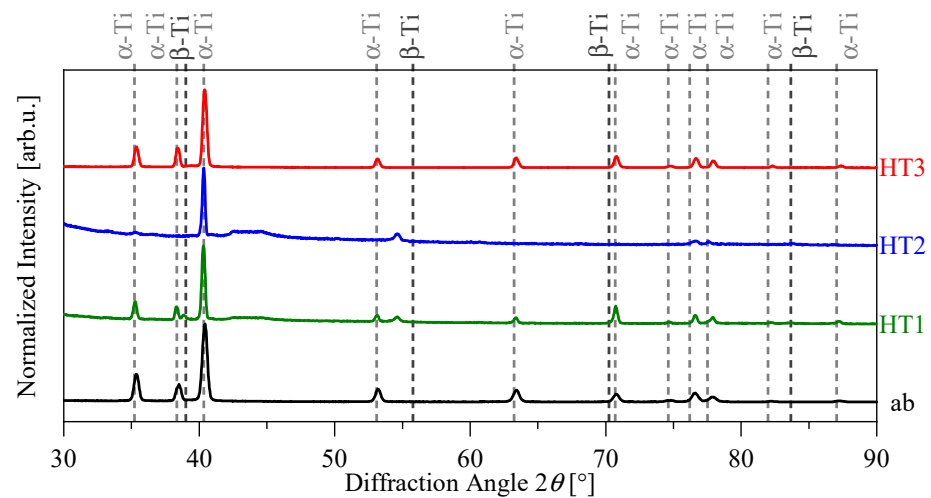


Figure 6. XRD patterns of as-built and heat-treated Ti-6Al-7Nb samples.

Table 1. Phase fraction detected by means of EBSD and results of quasi-static and fatigue tests of the LPBF fabricated, as-built, and heat-treated Ti-6Al-7Nb, including the minimum values regarding standard ISO 5832-11 [92].

State	Condition	α Phase	β Phase	$R_{p0.2}$ [MPa]	R_m [MPa]	E [GPa]	A [%]	σ'_f	b	ϵ'_f	c
ab	as-built	97.0%	3.0%	940 ± 14	1109 ± 3	105 ± 3	14.4 ± 0.9	89.7	−0.102	765.04	−1.518
HT1	925 °C/4 h	98.3%	1.7%	870 ± 11	934 ± 7	108 ± 6	8.8 ± 2.3	49.9	−0.027	191.97	−1.166
HT2	1050 °C/2 h	97.8%	2.2%	718 ± 4	791 ± 6	115 ± 3	12.0 ± 1.1	52.2	−0.036	10.103	−0.719
HT3	600 °C/4 h	97.7%	2.3%	1045 ± 9	1110 ± 10	116 ± 2	12.5 ± 0.9	100.7	−0.097	139.84	−1.167
ISO	—	—	—	800	900	—	10	—	—	—	—

3.2. Mechanical Properties of Ti-6Al-7Nb

Figure 7 displays the results for different mechanical properties of the monotonic tensile tests with images of fracture surfaces. The stress–strain curves for the monotonic test are presented in Figure 7a. For the different conditions, the mean values of Young’s moduli, E, tensile yield strengths, $R_{p0.2}$, ultimate tensile strengths, R_m , and plastic elongations, A, are compared to the international standard for implants for surgery ISO 5832-11 in Figure 7c and Table 1 [92]. The martensitic structure of the additively processed ($\alpha + \beta$) titanium leads to high values for the mechanical properties regarding ultimate tensile and yield strength compared with wrought and conventionally processed materials, especially with an α -dominant equiaxed microstructure [7]. The different material behavior might be explained by the different microstructures and phase composition, which have a strong impact on the mechanical properties. Typically, in conventional material, the size and morphology of the α grains determine the mechanical properties, while in LPBF the colony size and the size of the α or rather α' laths control the properties. Plastic deformation tends to be the movement of dislocations. Conventional material with larger α grains enables the deformation with less dislocation pileups, whereas the smaller grains in the additively processed material increase the dislocation pileups [93]. The tensile properties are, inter alia, caused by the higher residual stresses, the martensitic transformation during fast cooling to the α' instead of the α phase, and grain refinement as a strengthening mechanism described by the Hall–Petch equation [94]. The Young’s moduli vary within a certain range between 105 GPa–116 GPa. Due to heat treatments and microstructural changes, the average grain size increases. Sliding effects are mainly detected between grains; therefore, the breaking elongation should increase [95]. Another reason for changes in breaking elongation is the presence of β titanium. An increased amount of bcc β titanium should improve the ductile behavior [57,95]. EBSD phase analysis showed the highest fraction of β titanium for as-built conditions (3.0%), the lowest fraction for HT1 (1.7%), and between for HT2 (2.2%)

and HT3 (2.3%), in accordance to the breaking elongation, see Figure 7c. According to the XRD analysis only for HT1 and HT2 β titanium is verified and may, therefore, explain the lower tensile strength for these conditions but not the reduced breaking elongations.

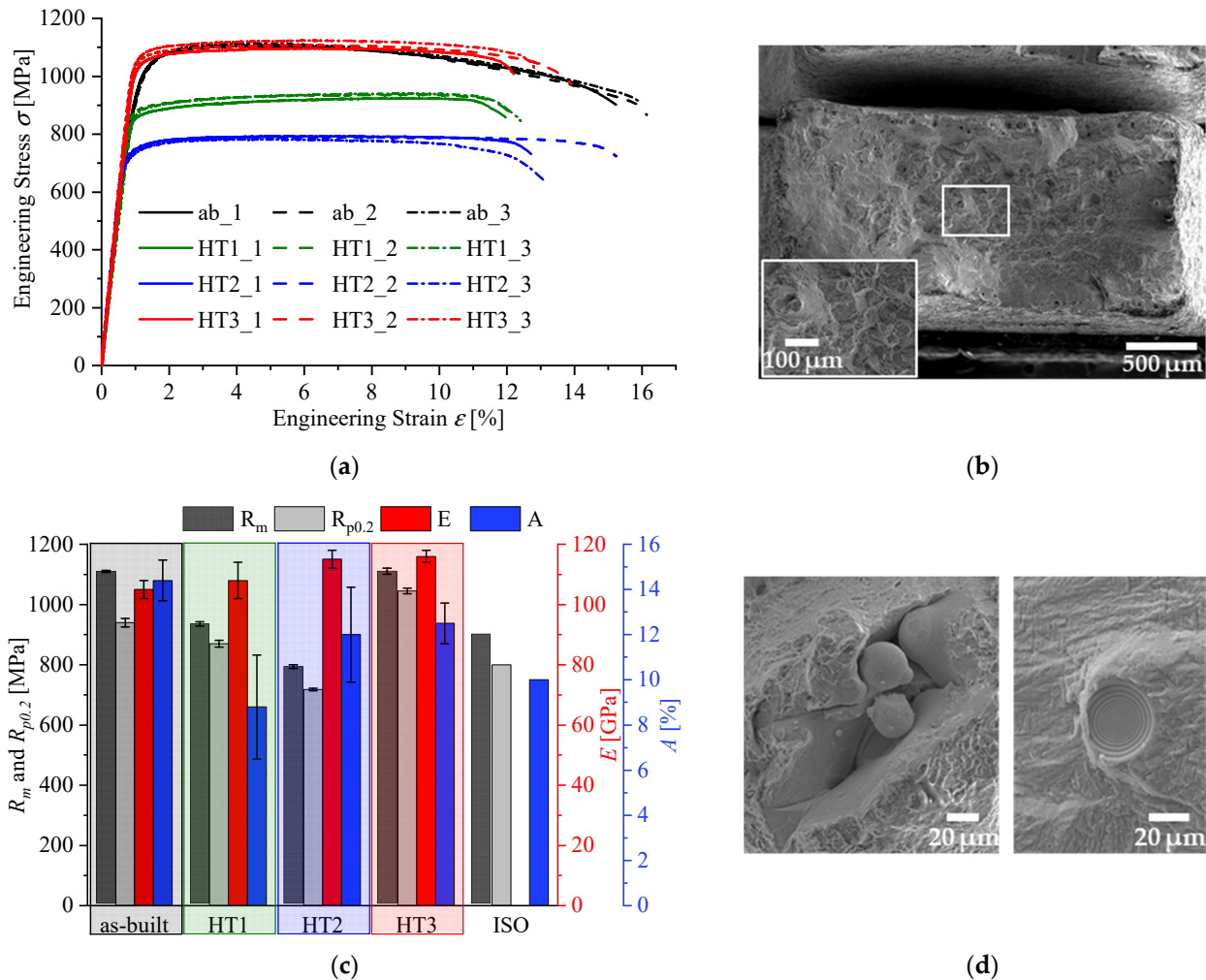


Figure 7. (a) Stress–strain curves of the as-built and heat-treated samples; (b) SEM images of the tensile fracture surface of an as-built Ti-6Al-7Nb specimen; (c) mechanical properties of the different conditions including minimum values for Ti-6Al-7Nb according to ISO 5832-11 (ISO) [92]; (d) SEM images of a characteristic LPBF defects, lack of fusion with unmelted powder particles (left) and gas pore (right), on a tensile fracture surface of an as-built Ti-6Al-7Nb specimen.

The ε_A - N_f plots for the different conditions are approximated with the Coffin–Manson–Basquin relation based on the elastic and plastic strain superposition explained in Figure 2. The results are depicted in Figure 8a. The approximations represent the relation between the total strain ε_A and the fatigue life N_f of Ti-6Al-7Nb alloy in different conditions. The Coffin–Manson–Basquin fatigue life approximation are determined as follows:

$$\varepsilon_{A, \text{as-built}} = 765.04 \cdot (2N_f)^{-1.518} + 0.8545 \cdot (2N_f)^{-0.102}; \quad (6)$$

$$\varepsilon_{A, \text{HT1}} = 191.97 \cdot (2N_f)^{-1.166} + 0.4616 \cdot (2N_f)^{-0.027}; \quad (7)$$

$$\varepsilon_{A, \text{HT2}} = 10.103 \cdot (2N_f)^{-0.719} + 0.4535 \cdot (2N_f)^{-0.036}; \quad (8)$$

$$\varepsilon_{A, \text{HT3}} = 139.84 \cdot (2N_f)^{-1.167} + 0.8677 \cdot (2N_f)^{-0.097}. \quad (9)$$

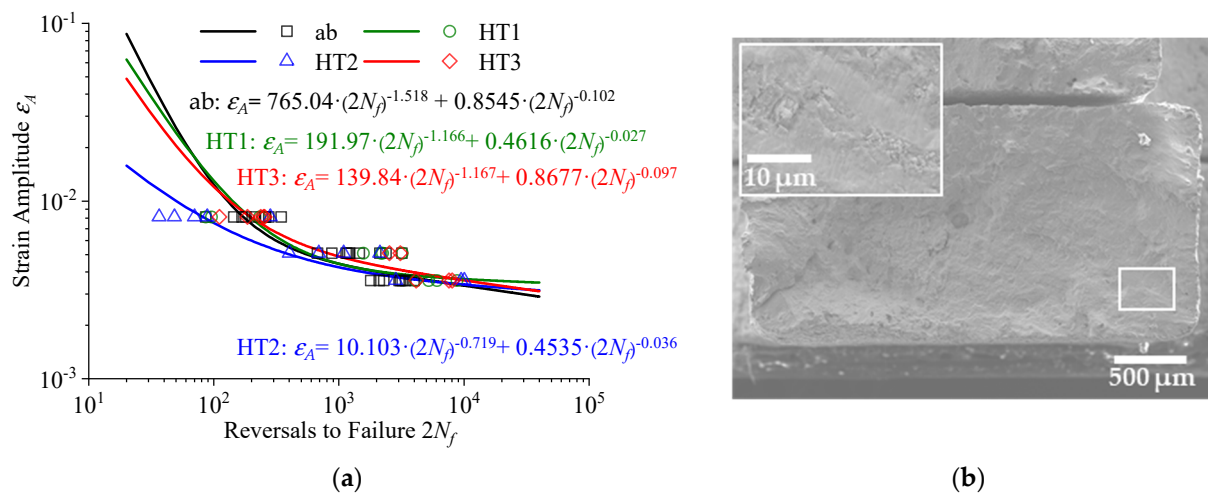


Figure 8. (a) Coffin–Manson–Basquin plots for Ti-6Al-7Nb samples in as-built, HT1, HT2, and HT3 conditions; (b) SEM images of a fracture surface of an as-built Ti-6Al-7Nb fatigue specimens, with fatigue striations, probably oriented perpendicular to the crack growth direction.

Figure 8a depicts the fatigue life of the different conditions. The fatigue performance for higher strain amplitudes ($2N_f < 10^2$ reversals) of the as-built condition is better, compared with the HT1, HT2, and HT3 conditions. The fatigue performance in LCF range is connected to the monotonic tensile performance in terms of tensile strength. Higher strengths tend to lead to higher, tolerable strain amplitudes and higher fatigue life. Fatigue strength is generally high as higher monotonic strength hinders microplasticity and eventually local damage [42]. The curves of the as-built HT1 and HT3 conditions intersect around 10^2 cycles and are comparable up to 10^4 cycles. While the performance for higher strain amplitudes ($2N_f < 10^4$ reversals) for the HT2 condition is the worst, the performance gets better for lower strain amplitudes. As the process-induced pores and defects are not affected by these post-treatments, other causes are likely to be decisive, such as the microstructures or residual stresses. For post treatment HT2 the reduced strength and the microstructural notches could lead to accumulation of local damage and finally results in early crack initiation [42]. The fatigue crack growth behavior of post-treated Ti-6Al-7Nb is affected by the microstructure. Depending on the crack growth direction and grain long axis different crack growth rates are probable [96–98]. For lower strain amplitudes, the three heat-treated conditions show superior fatigue behavior compared with the as-built conditions, attributed to the reduced residual stresses and microstructural features [52,56–59,94]. Corresponding to the fatigue ductility exponent c , the heat-treated specimens show smaller gradients, while the as-built condition has the lowest value resulting in the shortest fatigue life. HT1 and HT3 exhibit close fatigue ductility exponent c and, therefore, are probably favorable for HCF applications.

In general, due to miniaturization of samples the fatigue and monotonic tensile behavior could be affected [42]. The monotonic material properties, such as Young's moduli E , tensile yield strengths $R_{p0,2}$, ultimate tensile strengths R_m , plastic elongations A , the fatigue parameters—such as fatigue strength coefficients σ'_f and exponents b —and fatigue ductility coefficients ϵ'_f and exponents c , of the Coffin–Manson–Basquin equation, are given in Table 1.

3.3. Fracture Behavior

The fracture surface of the as-built Ti-6Al-7Nb alloy demonstrates mainly ductile fracture behavior, see Figure 7b. The propensity of cleavage fracture decreases with decreasing grain size. Therefore, the fracture surface of the additively processed materials shows cleavage facets with high amounts of dimples at the grain boundaries [58]. These fractured surfaces show small, shallow dimples on quasi-cleavage fracture surfaces, and transgran-

ular facets, confirming the minor brittle fracture behavior of the additively processed specimens. Features, as a result of the LPBF fabrication, such as pores, unmelted powder particles, and defects occur on fracture surfaces in as-built and heat-treated conditions, see Figure 7d. These build defects typically are perpendicular to the build direction and pulled apart by the tensile load during monotonic and fatigue tests [99,100]. The fracture surfaces of fatigue tests tend to be smoother for lower strain amplitudes. Distinct fatigue striations, perpendicular to the crack growth direction, can be detected for all conditions and strain amplitudes, see Figure 8b. The striations are close to the probable crack initiation spot. Typical forced rupture areas are difficult to spot.

3.4. Characterization of Roughness, Cytocompatibility, and Antibacterial Effects

The roughness of the specimens without surface treatment (NT) exhibits values for Ra of $7.5 \pm 0.3 \mu\text{m}$ and Rz of $49.6 \pm 2.2 \mu\text{m}$. Due to unmelted powder particles and the surface of the layer-wise fabrication, the roughness of NT specimens is higher than for the blasted specimens (ab) with Ra of $4.8 \pm 0.2 \mu\text{m}$ and Rz of $34.3 \pm 1.2 \mu\text{m}$, which have smoother surfaces, on account of the mechanically post-processed treatment.

There was no effect of cell proliferation of the two examined samples on murine L-929 cells and human HUVEC cells. A slight tendency of diminished cell proliferation was observed in human HOS cells on blasted Ti-6Al-7Nb. Thus, the examined samples show a proper biocompatibility behavior for the different cell lines, used in the present study, see Figure 9. Furthermore, no increase in cytokine release of Il-6 was detected (data not shown). Concerning antibacterial effects, *E. coli* proliferation was not influenced by the different samples, while the proliferation of *S. aureus* was reduced by the blasted surface of Ti-6Al-7Nb, see Figure 9.

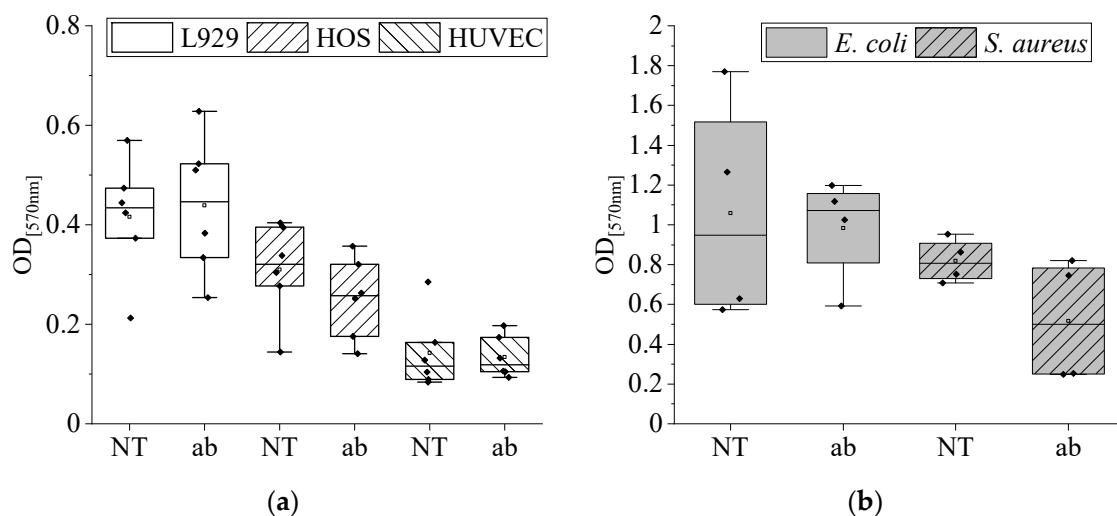


Figure 9. (a) Effects of different surfaces on the proliferation of L929, HOS and HUVEC cells after 72 h incubation, and (b) bacterial proliferation of *E. coli* and *S. aureus* after 24 h incubation; OD = optical density at 570 nm; $n = 4-6$.

As described by Schweickl et al., blasting with Al_2O_3 particles led to incorporation of Al into the outer surface layers [101]. Therefore, the increased concentration of Al on the specimens' surfaces could result in decreasing the proliferation behavior of HOS cells and *S. aureus* [102–104]. Rough sandblasted surfaces with sharp ridges and edges could influence the proliferation and it seems to appear that the quality of cell contact on rough surfaces is related to the minimum width of the cavity [101]. As reported in various studies, blasting leads to the presence of severely plastic deformed layers and, therefore, to strain-hardening, as well as to compressive residual stresses [105–107]. Due to the antibacterial effect regarding the proliferation of *S. aureus* and because of probably

better fatigue properties of blasted specimens, the specimens for the mechanical tests were blasted with Al_2O_3 particles.

4. Conclusions

The microstructure and the monotonic and fatigue behaviors of additively processed Ti-6Al-7Nb were investigated. Different surface conditions were examined regarding biocompatible properties, such as cytocompatibility and antibacterial effects. The following conclusions can be drawn from these investigations:

- Ti-6Al-7Nb shows significantly different microstructures in the as-built, stress-relieved, recrystallized, and β -annealed conditions. While the α'/α structure is dominant within the as-built state, the formation and precipitation of the β -phase are manageable by a vacuum heat treatment above 925 °C as analyzed using XRD and EBSD.
- There are significant differences in the monotonic tensile properties of the various conditions. Concerning the ISO values, the as-built and stress-relieved conditions (HT3) are favorable. Tensile and yield strength, as well as breaking elongation, are higher than the demanded values, but the specimens' dimensions have to be considered. HT1 and HT2 do not fulfill the requirements, probably due to the present β -phase. Heat treatments, such as HT1 and HT2, can significantly affect the microstructure and may tend to soften the lattice structures and decrease the residual stresses and, therefore, lead to significantly reduced tensile strength.
- LCF life is higher for lower strain amplitudes in the heat-treated specimens than in as-built conditions, which can be attributed to decreased residual stresses as well as to microstructural differences. HT2 shows the highest fatigue life for lower strain amplitudes, while the as-built condition has higher service life for higher strain amplitudes. Regarding overall performance, quasi-static results, and LCF performance, stress relief treatment (HT3) is favorable. The material behavior for HCF loading still has to be determined.
- Transgranular facets characterize the fracture surface of the additively processed Ti-6Al-7Nb, confirming the ductile behavior. Small, shallow dimples on quasi-cleavage fracture surfaces are visible. Fatigue fracture surfaces are characterized by fatigue striations and remaining forced rupture surfaces. Defects may have less impact on quasi-static but a high impact on fatigue behavior.
- Both surfaces, the untreated and the blasted, show good biocompatibility in different cell types (fibroblasts, osteosarcoma cells, and endothelial cells). Only a slight anti-proliferative effect was observed for blasted Ti-6Al-7Nb in osteoblasts. An increase in cytokine release of Il-6 was not observed.
- Blasting with high-grade Al_2O_3 is preferable regarding biocompatibility and antibacterial effects. Blasted Ti-6Al-7Nb exhibits an antibacterial effect against *S. aureus* in comparison with not post-treated Ti-6Al-7Nb. *E. coli* was able to grow on both surfaces of Ti-6Al-7Nb similarly. On account of remaining aluminum on the blasted surface, glass bead blasting could be taken into consideration.

Author Contributions: Conceptualization, M.H., K.-P.H. and M.S.; data curation, M.H.; formal analysis, M.H., K.-P.H. and M.S.; funding acquisition, K.-P.H., J.M., W.T. and M.S.; investigation, M.H., D.K., N.F.L.D., D.S., H.O., S.P. and J.M.; methodology, M.H., K.-P.H. and M.S.; project administration, M.H.; resources, J.M., W.T. and M.S.; software, M.H. and D.K.; supervision, K.-P.H., J.M., W.T. and M.S.; validation, M.H., K.-P.H. and M.S.; visualization, M.H.; writing—original draft preparation, M.H.; writing—review and editing, M.H., D.K., N.F.L.D., D.S., H.O., S.P., M.K., K.-P.H., J.M., W.T. and M.S. All authors have read and agreed to the published version of the manuscript.

Funding: This research was funded by the Deutsche Forschungsgemeinschaft (DFG), grant numbers SCHA 1484/45-1, ME 4991/2-1 and TI 343/167-1.

Data Availability Statement: The data that support the findings of this study are available from the corresponding author upon reasonable request.

Acknowledgments: The research was performed with the equipment and base of the LWK and DMRC research infrastructure. The authors are grateful to the staff members of the LWK and DMRC.

Conflicts of Interest: The authors declare no conflict of interest. The funders had no role in the design of the study; in the collection, analyses, or interpretation of data; in the writing of the manuscript, or in the decision to publish the results.

References

1. Abdel-Hady Gepreel, M.; Niinomi, M. Biocompatibility of Ti-alloys for long-term implantation. *J. Mech. Behav. Biomed. Mater.* **2013**, *20*, 407–415. [[CrossRef](#)] [[PubMed](#)]
2. Geetha, M.; Singh, A.K.; Asokamani, R.; Gogia, A.K. Ti based biomaterials, the ultimate choice for orthopaedic implants—A review. *Prog. Mater. Sci.* **2009**, *54*, 397–425. [[CrossRef](#)]
3. Long, M.; Rack, H. Titanium alloys in total joint replacement—A materials science perspective. *Biomaterials* **1998**, *19*, 1621–1639. [[CrossRef](#)]
4. Kurtz, S.M.; Ong, K.L.; Schmier, J.; Mowat, F.; Saleh, K.; Dybvik, E.; Kärrholm, J.; Garellick, G.; Havelin, L.I.; Furnes, O.; et al. Future clinical and economic impact of revision total hip and knee arthroplasty. *J. Bone Jt. Surg. Am.* **2007**, *89* (Suppl. S3), 144–151. [[CrossRef](#)]
5. Vandenbroucke, B.; Kruth, J.-P. Selective laser melting of biocompatible metals for rapid manufacturing of medical parts. *Rapid Prototyp. J.* **2007**, *13*, 196–203. [[CrossRef](#)]
6. Iijima, D. Wear properties of Ti and Ti–6Al–7Nb castings for dental prostheses. *Biomaterials* **2003**, *24*, 1519–1524. [[CrossRef](#)]
7. Niinomi, M. Mechanical biocompatibilities of titanium alloys for biomedical applications. *J. Mech. Behav. Biomed. Mater.* **2008**, *1*, 30–42. [[CrossRef](#)]
8. Hollander, D.A.; von Walter, M.; Wirtz, T.; Sellei, R.; Schmidt-Rohlfing, B.; Paar, O.; Erli, H.-J. Structural, mechanical and in vitro characterization of individually structured Ti-6Al-4V produced by direct laser forming. *Biomaterials* **2006**, *27*, 955–963. [[CrossRef](#)] [[PubMed](#)]
9. Murr, L.E.; Quinones, S.A.; Gaytan, S.M.; Lopez, M.I.; Rodela, A.; Martinez, E.Y.; Hernandez, D.H.; Martinez, E.; Medina, F.; Wicker, R.B. Microstructure and mechanical behavior of Ti-6Al-4V produced by rapid-layer manufacturing, for biomedical applications. *J. Mech. Behav. Biomed. Mater.* **2009**, *2*, 20–32. [[CrossRef](#)]
10. Kobayashi, E.; Wang, T.J.; Doi, H.; Yoneyama, T.; Hamanaka, H. Mechanical properties and corrosion resistance of Ti-6Al-7Nb alloy dental castings. *J. Mater. Sci. Mater. Med.* **1998**, *9*, 567–574. [[CrossRef](#)]
11. Kobayashi, E.; Mochizuki, H.; Doi, H.; Yoneyama, T.; Hanawa, T. Fatigue Life Prediction of Biomedical Titanium Alloys under Tensile/Torsional Stress. *Mater. Trans.* **2006**, *47*, 1826–1831. [[CrossRef](#)]
12. Srimaneepong, V.; Yoneyama, T.; Kobayashi, E.; Doi, H.; Hanawa, T. Comparative study on torsional strength, ductility and fracture characteristics of laser-welded alpha+beta Ti-6Al-7Nb alloy, CP Titanium and Co-Cr alloy dental castings. *Dent. Mater.* **2008**, *24*, 839–845. [[CrossRef](#)]
13. Liu, X.; Chu, P.; Ding, C. Surface modification of titanium, titanium alloys, and related materials for biomedical applications. *Mater. Sci. Eng. R Rep.* **2004**, *47*, 49–121. [[CrossRef](#)]
14. Kuroda, D.; Niinomi, M.; Morinaga, M.; Kato, Y.; Yashiro, T. Design and mechanical properties of new β type titanium alloys for implant materials. *Mater. Sci. Eng. A Struct. Mater.* **1998**, *243*, 244–249. [[CrossRef](#)]
15. Li, Y.; Yang, C.; Zhao, H.; Qu, S.; Li, X.; Li, Y. New Developments of Ti-Based Alloys for Biomedical Applications. *Materials* **2014**, *7*, 1709–1800. [[CrossRef](#)]
16. López, M.; Gutiérrez, A.; Jiménez, J. In vitro corrosion behaviour of titanium alloys without vanadium. *Electrochim. Acta* **2002**, *47*, 1359–1364. [[CrossRef](#)]
17. Chlebus, E.; Kuźnicka, B.; Kurzynowski, T.; Dybała, B. Microstructure and mechanical behaviour of Ti–6Al–7Nb alloy produced by selective laser melting. *Mater. Charact.* **2011**, *62*, 488–495. [[CrossRef](#)]
18. Surmeneva, M.; Grubova, I.; Glukhova, N.; Khrapov, D.; Koptuyug, A.; Volkova, A.; Ivanov, Y.; Cotrut, C.M.; Vladescu, A.; Teresov, A.; et al. New Ti–35Nb–7Zr–5Ta Alloy Manufacturing by Electron Beam Melting for Medical Application Followed by High Current Pulsed Electron Beam Treatment. *Metals* **2021**, *11*, 1066. [[CrossRef](#)]
19. Tamilselvi, S.; Raman, V.; Rajendran, N. Corrosion behaviour of Ti–6Al–7Nb and Ti–6Al–4V ELI alloys in the simulated body fluid solution by electrochemical impedance spectroscopy. *Electrochim. Acta* **2006**, *52*, 839–846. [[CrossRef](#)]
20. Metikoš-Huković, M.; Kwokal, A.; Piljac, J. The influence of niobium and vanadium on passivity of titanium-based implants in physiological solution. *Biomaterials* **2003**, *24*, 3765–3775. [[CrossRef](#)]
21. Schmidt, M.; Merklein, M.; Bourell, D.; Dimitrov, D.; Hausotte, T.; Wegener, K.; Overmeyer, L.; Vollertsen, F.; Levy, G.N. Laser based additive manufacturing in industry and academia. *CIRP Ann.* **2017**, *66*, 561–583. [[CrossRef](#)]
22. Bourell, D.; Kruth, J.P.; Leu, M.; Levy, G.; Rosen, D.; Beese, A.M.; Clare, A. Materials for additive manufacturing. *CIRP Ann.* **2017**, *66*, 659–681. [[CrossRef](#)]
23. Wohlers, T.T.; Campbell, I.; Diegel, O.; Kowen, J. *Wohlers Report 2018. 3D Printing and Additive Manufacturing State of the Industry: Annual Worldwide Progress Report*; Wohlers Associates, Inc.: Fort Collins, CO, USA, 2018; ISBN 0991333241.

24. Attar, H.; Prashanth, K.G.; Chaubey, A.K.; Calin, M.; Zhang, L.C.; Scudino, S.; Eckert, J. Comparison of wear properties of commercially pure titanium prepared by selective laser melting and casting processes. *Mater. Lett.* **2015**, *142*, 38–41. [[CrossRef](#)]
25. Dai, N.; Zhang, L.-C.; Zhang, J.; Chen, Q.; Wu, M. Corrosion behavior of selective laser melted Ti-6Al-4 V alloy in NaCl solution. *Corros. Sci.* **2016**, *102*, 484–489. [[CrossRef](#)]
26. Yang, Y.; Chen, Y.; Zhang, J.; Gu, X.; Qin, P.; Dai, N.; Li, X.; Kruth, J.-P.; Zhang, L.-C. Improved corrosion behavior of ultrafine-grained eutectic Al-12Si alloy produced by selective laser melting. *Mater. Des.* **2018**, *146*, 239–248. [[CrossRef](#)]
27. Melchels, F.P.; Domingos, M.A.; Klein, T.J.; Malda, J.; Bartolo, P.J.; Huttmacher, D.W. Additive manufacturing of tissues and organs. *Prog. Polym. Sci.* **2012**, *37*, 1079–1104. [[CrossRef](#)]
28. Herzog, D.; Seyda, V.; Wycisk, E.; Emmelmann, C. Additive manufacturing of metals. *Acta Mater.* **2016**, *117*, 371–392. [[CrossRef](#)]
29. Guo, N.; Leu, M.C. Additive manufacturing: Technology, applications and research needs. *Front. Mech. Eng.* **2013**, *8*, 215–243. [[CrossRef](#)]
30. Lewandowski, J.J.; Seifi, M. Metal Additive Manufacturing: A Review of Mechanical Properties. *Annu. Rev. Mater. Res.* **2016**, *46*, 151–186. [[CrossRef](#)]
31. Yap, C.Y.; Chua, C.K.; Dong, Z.L.; Liu, Z.H.; Zhang, D.Q.; Loh, L.E.; Sing, S.L. Review of selective laser melting: Materials and applications. *Appl. Phys. Rev.* **2015**, *2*, 41101. [[CrossRef](#)]
32. Tolosa, I.; Garciandía, F.; Zubiri, F.; Zapirain, F.; Esnaola, A. Study of mechanical properties of AISI 316 stainless steel processed by “selective laser melting”, following different manufacturing strategies. *Int. J. Adv. Manuf. Technol.* **2010**, *51*, 639–647. [[CrossRef](#)]
33. Nezhadfar, P.D.; Burford, E.; Anderson-Wedge, K.; Zhang, B.; Shao, S.; Daniewicz, S.R.; Shamsaei, N. Fatigue crack growth behavior of additively manufactured 17-4 PH stainless steel: Effects of build orientation and microstructure. *Int. J. Fatigue* **2019**, *123*, 168–179. [[CrossRef](#)]
34. Kluczyński, J.; Śniezek, L.; Grzelak, K.; Torzewski, J.; Szachogłuchowicz, I.; Wachowski, M.; Łuszczek, J. Crack Growth Behavior of Additively Manufactured 316L Steel-Influence of Build Orientation and Heat Treatment. *Materials* **2020**, *13*, 3259. [[CrossRef](#)]
35. Zhang, M.; Sun, C.-N.; Zhang, X.; Wei, J.; Hardacre, D.; Li, H. High cycle fatigue and ratcheting interaction of laser powder bed fusion stainless steel 316L: Fracture behaviour and stress-based modelling. *Int. J. Fatigue* **2019**, *121*, 252–264. [[CrossRef](#)]
36. Jerrard, P.G.E.; Hao, L.; Evans, K.E. Experimental investigation into selective laser melting of austenitic and martensitic stainless steel powder mixtures. *Proc. Inst. Mech. Eng. B J. Eng. Manuf.* **2009**, *223*, 1409–1416. [[CrossRef](#)]
37. Baufeld, B.; Brandl, E.; van der Biest, O. Wire based additive layer manufacturing: Comparison of microstructure and mechanical properties of Ti-6Al-4V components fabricated by laser-beam deposition and shaped metal deposition. *J. Mater. Process. Technol.* **2011**, *211*, 1146–1158. [[CrossRef](#)]
38. Brandl, E. *Microstructural and Mechanical Properties of Additive Manufactured Titanium (Ti-6Al-4V) Using Wire. Evaluation with Respect to Additive Processes Using Powder and Aerospace Material Specifications*; Dissertation, Brandenburg University of Technology Cottbus-Senftenberg: Cottbus, Germany, 2010; ISBN 978-3-8322-9530-1.
39. Khorasani, A.; Gibson, I.; Goldberg, M.; Littlefair, G. On the role of different annealing heat treatments on mechanical properties and microstructure of selective laser melted and conventional wrought Ti-6Al-4V. *Rapid Prototyp. J.* **2017**, *23*, 295–304. [[CrossRef](#)]
40. Liu, S.; Shin, Y.C. Additive manufacturing of Ti6Al4V alloy: A review. *Mater. Des.* **2019**, *164*, 107552. [[CrossRef](#)]
41. Riemer, A.; Richard, H.A. Crack Propagation in Additive Manufactured Materials and Structures. *Procedia Struct. Integr.* **2016**, *2*, 1229–1236. [[CrossRef](#)]
42. Leuders, S.; Lieneke, T.; Lammers, S.; Tröster, T.; Niendorf, T. On the fatigue properties of metals manufactured by selective laser melting—The role of ductility. *J. Mater. Res.* **2014**, *29*, 1911–1919. [[CrossRef](#)]
43. Tillmann, W.; Hagen, L.; Garthe, K.-U.; Hoyer, K.-P.; Schaper, M. Effect of substrate pre-treatment on the low cycle fatigue performance of tungsten carbide-cobalt coated additive manufactured 316 L substrates. *Mater. Werkst.* **2020**, *51*, 1452–1464. [[CrossRef](#)]
44. Romano, S.; Patriarca, L.; Foletti, S.; Beretta, S. LCF behaviour and a comprehensive life prediction model for AlSi10Mg obtained by SLM. *Int. J. Fatigue* **2018**, *117*, 47–62. [[CrossRef](#)]
45. Bressan, S.; Ogawa, F.; Itoh, T.; Berto, F. Low cycle fatigue behavior of additively manufactured Ti-6Al-4V under non-proportional and proportional loading. *Frat. Integrita Strutt.* **2019**, *13*, 18–25. [[CrossRef](#)]
46. Zhang, S.Q.; Li, S.J.; Jia, M.T.; Prima, F.; Chen, L.J.; Hao, Y.L.; Yang, R. Low-cycle fatigue properties of a titanium alloy exhibiting nonlinear elastic deformation behavior. *Acta Mater.* **2011**, *59*, 4690–4699. [[CrossRef](#)]
47. Awd, M.; Tenkamp, J.; Hirtler, M.; Siddique, S.; Bambach, M.; Walther, F. Comparison of Microstructure and Mechanical Properties of Scalmalloy® Produced by Selective Laser Melting and Laser Metal Deposition. *Materials* **2017**, *11*, 17. [[CrossRef](#)]
48. Leuders, S.; Thöne, M.; Riemer, A.; Niendorf, T.; Tröster, T.; Richard, H.A.; Maier, H.J. On the mechanical behaviour of titanium alloy TiAl6V4 manufactured by selective laser melting: Fatigue resistance and crack growth performance. *Int. J. Fatigue* **2013**, *48*, 300–307. [[CrossRef](#)]
49. Wycisk, E.; Siddique, S.; Herzog, D.; Walther, F.; Emmelmann, C. Fatigue Performance of Laser Additive Manufactured Ti-6Al-4V in Very High Cycle Fatigue Regime up to 109 Cycles. *Front. Mater.* **2015**, *2*, 72. [[CrossRef](#)]
50. Polozov, I.; Sufiiarov, V.; Popovich, A.; Masaylo, D.; Grigoriev, A. Synthesis of Ti-5Al, Ti-6Al-7Nb, and Ti-22Al-25Nb alloys from elemental powders using powder-bed fusion additive manufacturing. *J. Alloy. Compd.* **2018**, *763*, 436–445. [[CrossRef](#)]
51. Affolter, C.; Thorwarth, G.; Arabi-Hashemi, A.; Müller, U.; Weisse, B. Ductile Compressive Behavior of Biomedical Alloys. *Metals* **2020**, *10*, 60. [[CrossRef](#)]

52. Xu, C.; Sikan, F.; Atabay, S.E.; Muñiz-Lerma, J.A.; Sanchez-Mata, O.; Wang, X.; Brochu, M. Microstructure and mechanical behavior of as-built and heat-treated Ti-6Al-7Nb produced by laser powder bed fusion. *Mater. Sci. Eng. A Struct. Mater.* **2020**, *793*, 139978. [[CrossRef](#)]
53. Hein, M.; Hoyer, K.-P.; Schaper, M. Additively processed TiAl6Nb7 alloy for biomedical applications. *Mater. Werkst.* **2021**, *52*, 703–716. [[CrossRef](#)]
54. Bergmann, G.; Bender, A.; Dymke, J.; Duda, G.; Damm, P. Standardized Loads Acting in Hip Implants. *PLoS ONE* **2016**, *11*, e0155612. [[CrossRef](#)]
55. Bergmann, G.; Graichen, F.; Rohlmann, A.; Bender, A.; Heinlein, B.; Duda, G.N.; Heller, M.O.; Morlock, M.M. Realistic loads for testing hip implants. *Biomed. Mater. Eng.* **2010**, *20*, 65–75. [[CrossRef](#)] [[PubMed](#)]
56. Sallica-Leva, E.; Caram, R.; Jardini, A.L.; Fogagnolo, J.B. Ductility improvement due to martensite α' decomposition in porous Ti-6Al-4V parts produced by selective laser melting for orthopedic implants. *J. Mech. Behav. Biomed. Mater.* **2016**, *54*, 149–158. [[CrossRef](#)] [[PubMed](#)]
57. Tao, P.; Li, H.; Huang, B.; Hu, Q.; Gong, S.; Xu, Q. Tensile behavior of Ti-6Al-4V alloy fabricated by selective laser melting: Effects of microstructures and as-built surface quality. *China Foundry* **2018**, *15*, 243–252. [[CrossRef](#)]
58. Gil Mur, F.X.; Rodríguez, D.; Planell, J.A. Influence of tempering temperature and time on the α' -Ti-6Al-4V martensite. *J. Alloy. Compd.* **1996**, *234*, 287–289. [[CrossRef](#)]
59. Liang, Z.; Sun, Z.; Zhang, W.; Wu, S.; Chang, H. The effect of heat treatment on microstructure evolution and tensile properties of selective laser melted Ti6Al4V alloy. *J. Alloy. Compd.* **2019**, *782*, 1041–1048. [[CrossRef](#)]
60. Donachie, M.J. *Titanium. A Technical Guide*, 2nd ed.; ASM International: Materials Park, OH, USA, 2000; ISBN 9780871706867.
61. Bachmann, F.; Hielscher, R.; Schaeben, H. Texture Analysis with MTEX—Free and Open Source Software Toolbox. *Solid State Phenom.* **2010**, *160*, 63–68. [[CrossRef](#)]
62. Plumtree, A. Cyclic stress–Strain response and substructure. *Int. J. Fatigue* **2001**, *23*, 799–805. [[CrossRef](#)]
63. Rice, R.C. *Fatigue Design Handbook*, 2nd ed.; Society of Automotive Engineers: Warrendale, PA, USA, 1988; ISBN 9780898830118.
64. Skelton, R.P.; Maier, H.J.; Christ, H.-J. The Bauschinger effect, Masing model and the Ramberg–Osgood relation for cyclic deformation in metals. *Mater. Sci. Eng. A Struct. Mater.* **1997**, *238*, 377–390. [[CrossRef](#)]
65. Nieslony, A.; Dsoki, C.; Kaufmann, H.; Krug, P. New method for evaluation of the Manson–Coffin–Basquin and Ramberg–Osgood equations with respect to compatibility. *Int. J. Fatigue* **2008**, *30*, 1967–1977. [[CrossRef](#)]
66. Basquin, O.H. The exponential law of endurance tests. *Am. Soc. Test. Mater.* **1910**, *10*, 625–630.
67. Coffin, L.F. A Study of the Effects of Cyclic Thermal Stresses on a Ductile Metal. *Trans. Am. Soc. Mech.* **1954**, *76*, 931–950.
68. Manson, S.S. *Behavior of Materials Under Conditions of Thermal Stress*; National Advisory Committee for Aeronautics: Edwards, CA, USA, 1953.
69. Suresh, S. *Fatigue of Materials*, 2nd ed.; Reprint; Cambridge Univ. Press: Cambridge, UK, 2004; ISBN 978-0-521-57847-9.
70. ASM International. *Fatigue and Fracture*, 10th ed.; 3. Print; ASM International: Materials Park, OH, USA, 2002; ISBN 9780871703859.
71. Schupbach, P.; Glauser, R.; Bauer, S. Al₂O₃ Particles on Titanium Dental Implant Systems following Sandblasting and Acid-Etching Process. *Int. J. Biomater.* **2019**, *2019*, 6318429. [[CrossRef](#)]
72. Le Guéhennec, L.; Soueidan, A.; Layrolle, P.; Amouriq, Y. Surface treatments of titanium dental implants for rapid osseointegration. *Dent. Mater.* **2007**, *23*, 844–854. [[CrossRef](#)] [[PubMed](#)]
73. Wennerberg, A.; Albrektsson, T.; Chrcanovic, B. Long-term clinical outcome of implants with different surface modifications. *Eur. J. Oral Implantol.* **2018**, *11* (Suppl. S1), S123–S136.
74. Yuda, A.W.; Supriadi, S.; Saragih, A.S. Surface modification of Ti-alloy based bone implant by sandblasting. In *The 4th Biomedical Engineering's Recent Progress in Biomaterials, Drugs Development, Health, and Medical Devices, Proceedings of the International Symposium of Biomedical Engineering (ISBE), Padang, Indonesia, 22–24 July 2019*; AIP Publishing: Melville, NY, USA, 2019; p. 20015.
75. Yurtttutan, M.E.; Keskin, A. Evaluation of the effects of different sand particles that used in dental implant roughened for osseointegration. *BMC Oral Health* **2018**, *18*, 47. [[CrossRef](#)]
76. Gillies, R.J.; Didier, N.; Denton, M. Determination of cell number in monolayer cultures. *Anal. Biochem.* **1986**, *159*, 109–113. [[CrossRef](#)]
77. Sercombe, T.; Jones, N.; Day, R.; Kop, A. Heat treatment of Ti-6Al-7Nb components produced by selective laser melting. *Rapid Prototyp. J.* **2008**, *14*, 300–304. [[CrossRef](#)]
78. Ajeel, S.A.; Alzubaydi, T.L.; Swadi, A.K. Influence of Heat Treatment Conditions on Microstructure of Ti-6Al-7Nb Alloy as Used Surgical Implant Materials. *Eng. Technol.* **2007**, *25*, 431–442.
79. DebRoy, T.; Wei, H.L.; Zuback, J.S.; Mukherjee, T.; Elmer, J.W.; Milewski, J.O.; Beese, A.M.; Wilson-Heid, A.; De, A.; Zhang, W. Additive manufacturing of metallic components—Process, structure and properties. *Prog. Mater. Sci.* **2018**, *92*, 112–224. [[CrossRef](#)]
80. Körner, C. Additive manufacturing of metallic components by selective electron beam melting—A review. *Int. Mater. Rev.* **2016**, *61*, 361–377. [[CrossRef](#)]
81. Banerjee, S.; Mukhopadhyay, P. *Phase Transformations. Examples from Titanium and Zirconium Alloys*; Elsevier: Amsterdam, The Netherlands; Oxford, UK, 2007; ISBN 9780080421452.
82. Thijs, L.; Verhaeghe, F.; Craeghs, T.; van Humbeeck, J.; Kruth, J.-P. A study of the microstructural evolution during selective laser melting of Ti-6Al-4V. *Acta Mater.* **2010**, *58*, 3303–3312. [[CrossRef](#)]

83. Kobryn, P.; Semiatin, S. Microstructure and texture evolution during solidification processing of Ti–6Al–4V. *J. Mater. Process. Technol.* **2003**, *135*, 330–339. [[CrossRef](#)]
84. Lütjering, G. Influence of processing on microstructure and mechanical properties of ($\alpha + \beta$) titanium alloys. *Mater. Sci. Eng. A Struct. Mater.* **1998**, *243*, 32–45. [[CrossRef](#)]
85. Lütjering, G.; Williams, J.C. *Titanium*, 2nd ed.; Springer: Berlin, Germany, 2007; ISBN 9783540713975.
86. Burgers, W.G. On the process of transition of the cubic-body-centered modification into the hexagonal-close-packed modification of zirconium. *Physica* **1934**, *1*, 561–586. [[CrossRef](#)]
87. Peters, M.; Leyens, C. *Titan und Titanlegierungen*, 3rd ed.; Wiley-VCH: Weinheim, Germany, 2002; ISBN 9783527611089.
88. Murr, L.E.; Gaytan, S.M.; Ramirez, D.A.; Martinez, E.; Hernandez, J.; Amato, K.N.; Shindo, P.W.; Medina, F.R.; Wicker, R.B. Metal Fabrication by Additive Manufacturing Using Laser and Electron Beam Melting Technologies. *J. Mater. Sci. Technol.* **2012**, *28*, 1–14. [[CrossRef](#)]
89. Rehme, O. *Cellular Design for Laser Freeform Fabrication*, 1st ed.; Cuvillier Verlag: Göttingen, Germany, 2010; ISBN 9783869552736.
90. Sieniawski, J.; Ziaja, W.; Kubiak, K.; Motyk, M. Microstructure and Mechanical Properties of High Strength Two-Phase Titanium Alloys. In *Titanium Alloys—Advances in Properties Control*; Sieniawski, J., Ziaja, W., Eds.; InTech: Rijeka, Croatia, 2014; ISBN 978-953-51-1110-8.
91. Bolzoni, L.; Weissgaerber, T.; Kieback, B.; Ruiz-Navas, E.M.; Gordo, E. Mechanical behaviour of pressed and sintered CP Ti and Ti-6Al-7Nb alloy obtained from master alloy addition powder. *J. Mech. Behav. Biomed. Mater.* **2013**, *20*, 149–161. [[CrossRef](#)] [[PubMed](#)]
92. *ISO 5832-11:2014; Chirurgische Implantate—Metallische Werkstoffe—Teil 11: Titan Aluminium-6 Niob-7 Knetlegierung*. DIN Deutsches Institut für Normung e. V.: Berlin, Germany, 2015.
93. Shunmugavel, M.; Polishetty, A.; Littlefair, G. Microstructure and Mechanical Properties of Wrought and Additive Manufactured Ti-6Al-4V Cylindrical Bars. *Procedia Technol.* **2015**, *20*, 231–236. [[CrossRef](#)]
94. Attar, H.; Calin, M.; Zhang, L.C.; Scudino, S.; Eckert, J. Manufacture by selective laser melting and mechanical behavior of commercially pure titanium. *Mater. Sci. Eng. A Struct. Mater.* **2014**, *593*, 170–177. [[CrossRef](#)]
95. Gorny, B.; Niendorf, T.; Lackmann, J.; Thoene, M.; Troester, T.; Maier, H.J. In situ characterization of the deformation and failure behavior of non-stochastic porous structures processed by selective laser melting. *Mater. Sci. Eng. A Struct. Mater.* **2011**, *528*, 7962–7967. [[CrossRef](#)]
96. Blochwitz, C.; Jacob, S.; Tirschler, W. Grain orientation effects on the growth of short fatigue cracks in austenitic stainless steel. *Mater. Sci. Eng. A Struct. Mater.* **2008**, *496*, 59–66. [[CrossRef](#)]
97. Rao, K.T.V.; Yu, W.; Ritchie, R.O. Fatigue crack propagation in aluminum-lithium alloy 2090: Part II. small crack behavior. *Metall. Mater. Trans. A Phys. Metall. Mater. Sci.* **1988**, *19*, 563–569. [[CrossRef](#)]
98. Riemer, A.; Leuders, S.; Thöne, M.; Richard, H.A.; Tröster, T.; Niendorf, T. On the fatigue crack growth behavior in 316 L stainless steel manufactured by selective laser melting. *Eng. Fract. Mech.* **2014**, *120*, 15–25. [[CrossRef](#)]
99. Zerbst, U.; Bruno, G.; Buffiere, J.-Y.; Wegener, T.; Niendorf, T.; Wu, T.; Zhang, X.; Kashaev, N.; Meneghetti, G.; Hrabe, N.; et al. Damage tolerant design of additively manufactured metallic components subjected to cyclic loading: State of the art and challenges. *Prog. Mater. Sci.* **2021**, *121*, 100786. [[CrossRef](#)] [[PubMed](#)]
100. Afkhami, S.; Dabiri, M.; Alavi, S.H.; Björk, T.; Salminen, A. Fatigue characteristics of steels manufactured by selective laser melting. *Int. J. Fatigue* **2019**, *122*, 72–83. [[CrossRef](#)]
101. Schweikl, H.; Müller, R.; Englert, C.; Hiller, K.-A.; Kujat, R.; Nerlich, M.; Schmalz, G. Proliferation of osteoblasts and fibroblasts on model surfaces of varying roughness and surface chemistry. *J. Mater. Sci. Mater. Med.* **2007**, *18*, 1895–1905. [[CrossRef](#)] [[PubMed](#)]
102. Jeffery, E.H.; Abreo, K.; Burgess, E.; Cannata, J.; Greger, J.L. Systemic aluminum toxicity: Effects on bone, hematopoietic tissue, and kidney. *J. Toxicol. Environ. Health* **1996**, *48*, 649–665. [[CrossRef](#)] [[PubMed](#)]
103. Daley, B.; Doherty, A.T.; Fairman, B.; Case, C.P. Wear debris from hip or knee replacements causes chromosomal damage in human cells in tissue culture. *J. Bone Jt. Surg. Br.* **2004**, *86-B*, 598–606. [[CrossRef](#)]
104. Weng, Y.; Liu, H.; Ji, S.; Huang, Q.; Wu, H.; Li, Z.; Wu, Z.; Wang, H.; Tong, L.; Fu, R.K.; et al. A promising orthopedic implant material with enhanced osteogenic and antibacterial activity: Al₂O₃-coated aluminum alloy. *Appl. Surf. Sci.* **2018**, *457*, 1025–1034. [[CrossRef](#)]
105. Cattoni, D.; Ferrari, C.; Lebedev, L.; Pazos, L.; Svoboda, H. Effect of Blasting on the Fatigue Life of Ti-6Al-7Nb and Stainless Steel AISI 316 LVM. *Proc. Mater. Sci.* **2012**, *1*, 461–468. [[CrossRef](#)]
106. Javier Gil, F.; Planell, J.A.; Padrós, A.; Aparicio, C. The effect of shot blasting and heat treatment on the fatigue behavior of titanium for dental implant applications. *Dent. Mater.* **2007**, *23*, 486–491. [[CrossRef](#)] [[PubMed](#)]
107. Pazos, L.; Corengia, P.; Svoboda, H. Effect of surface treatments on the fatigue life of titanium for biomedical applications. *J. Mech. Behav. Biomed. Mater.* **2010**, *3*, 416–424. [[CrossRef](#)] [[PubMed](#)]